The effect of donor content on the efficiency of P3HT:PCBM bilayers: optical and photocurrent spectral data analyses†

Mosé Casalegno,*[a] Dariusz Kotowski,[b] Andrea Bernardi,[c] Silvia Luzzati,[b] Riccardo Po[c] and Guido Raos[a]

Received 26th August 2014,
Accepted 27th November 2014

1 Introduction

Organic solar cells (OSCs) provide a potentially cheap and environmentally friendly way to address solar energy conversion.[1–5] The photoactive layer of these devices consists of two organic semiconductors, namely an electron donor (D) and an electron acceptor (A). The presence of two materials with complementary electronic properties is necessary in order to dissociate tightly bound excitons that form upon light absorption.[6] The way the donor and the acceptor are combined crucially affects device performance.[7,8] The two materials must be intimately mixed to overcome the short exciton diffusion length (typically 5–10 nm in organic semiconducting materials[9–13]). At the same time, however, the composite structure must provide continuous pathways for charge extraction.

The usual method to obtain such an interpenetrated D–A network, commonly referred to as the bulk-heterojunction (BHJ), is to cast a blend from a single solution of both components.[14] Post-processing treatments, such as thermal or solvent annealing,[15] are often used to optimize the phase separation and improve molecular organization within the individual phases.[16–18] This strategy has provided the most efficient OSCs to date.[19–22] The power conversion efficiencies (PCEs) resulting from its application depend on the identities of the D and A components but are also strongly affected by the processing conditions.[23–27] This, together with long-time ageing phenomena producing morphological changes, may represent an obstacle for the production of efficient and durable devices.

An alternative route for device preparation is that proposed by Ayzner and coworkers,[28] in which the polymer poly(3-hexylthiophene) (P3HT) and the soluble fullerene derivative phenyl-C61-butyric acid methyl ester (PCBM) are spin cast sequentially and separately using ''orthogonal solvents'', which dissolve selectively one or the other component.[29] These devices, often

[a] *Dipartimento di Chimica, Materiali e Ingegneria Chimica ''G. Natta'', Politecnico di Milano, Via L. Mancinelli 7, 20131 Milano, Italy. E-mail: mose.casalegno@polimi.it*
[b] *Istituto per lo Studio delle Macromolecole, Consiglio Nazionale delle Ricerche, Via Edoardo Bassini 15, 20133 Milano, Italy*
[c] *Research Center for Non-Conventional Energies, Istituto ENI Donegani, Eni S.p.A, Via G. Fauser 4, 28100 Novara, Italy*
† Electronic supplementary information (ESI) available.

referred to as bilayers, show PCEs of around 3.5%, thus comparable[30–32] or even higher[32] with those of BHJ devices based on the same materials. Bilayers can be expected to show a more favorable PCBM-rich composition at the free-air surface[33,34] and, therefore, better efficiencies.[35]

Motivated by the need to rationalize bilayer efficiencies and improve the understanding of P3HT:PCBM miscibility, several studies have focused on the morphology of sequentially deposited active layers.[31–33,36–40] It was found that the deposition of PCBM onto a P3HT film does not lead to a bilayer with a flat and sharp interface, as initially suggested.[28] Rather, even in the absence of thermal treatment, PCBM diffuses into and mixes with the P3HT layer,[31] resulting in a virtually constant concentration profile.[39,41] The process is likely to be assisted by the swelling of P3HT by the solvent used to deposit PCBM,[32,39] and occurs without disrupting the crystalline P3HT domains.[33,39] The last stage of this process may involve the reagglomeration of PCBM and the formation of pure PCBM domains within P3HT.[40] Whether the morphology resulting from sequential deposition is analogous to that obtained *via* conventional single solution processing is still a matter of debate.[32,37,38,42] In any case, it is clear that nanostructuring of the D–A blends should be taken into account in performance analysis of both BHJs and bilayers.

Among the various parameters that affect device efficiency, the active layer thickness and the D/A ratio are of key importance. These can be controlled, to a reasonable extent, by varying the concentration of the casting solution(s). Previous work on BHJs[14,43–46] has shown that increasing the active layer thickness generally improves photon absorption, although not monotonically, due to optical interference effects. At the same time, as the BHJ thickness is increased, charges have more chances to recombine at opposite sides of the D/A interface before reaching the corresponding electrodes. A similar trade-off was also found in bilayers where, under the assumption of a discrete D/A interface, the limiting factor for device efficiency was attributed to misbalanced carrier transit times, rather than to electron–hole recombination.[28] The optimal P3HT:PCBM volume ratio found in that work (4 : 1) was later confirmed in another study reported by Gevaerts *et al.*[32] Here, however, the possibility of a sharp D/A interface was rejected, based on the comparison between experimental and simulated external quantum efficiency (EQE) spectra. This study illustrates the benefits of a combined use of experimental and numerical approaches, in order to disentangle the many nanoscale phenomena underlying OSC behavior. Purely numerical studies based on Kinetic Monte Carlo, Master Equation or Drift-Diffusion simulations are also possible and they can provide useful insights.[47–49] However, these necessarily rely on assumptions about the device morphology and the elementary steps leading to the photogeneration of charges. These are still far from being clarified, as illustrated by the ongoing debate about the relative importance of "hot" *versus* "cold" exciton dissociation at D/A interfaces.[50–58]

Starting from the report of Campoy-Quiles *et al.*,[59] several experimental studies have highlighted a non-homogeneous vertical concentration profile in annealened P3HT:PCBM BHJ devices.[30,41,60,61] Different experimental techniques may produce different results,[60] but overall these have shown that annealing tends to produce an accumulation of PCBM at the underlying substrate (the anode), and to a lesser extent also at the air-film interface (before the final deposition of the cathode). In order to fully appreciate these results, it seems to be useful to place them within the broader context of polymer–nanoparticle blends,[62–64] in particular that of the self-assembly of nanoparticles at polymer interfaces.[65,66] A few years earlier, within a totally different context (influence of nanoparticles on the stability of polymer thin films against dewetting), Barnes *et al.*[67] had already shown that small nanoparticles such as C_{60} tend to segregate at an underlying substrate. The effect was generic, as it occurred for both polystyrene and polybutadiene, as well as chemically different nanoparticles. However, it does depend on nanoparticle size, so that it is eventually suppressed on replacing C_{60} with increasingly larger nanoparticles.[62,68] These features are consistent with classical density functional calculations[69,70] and molecular dynamics simulations[71] of coarse-grained polymer–nanoparticle models, which predicted a first-order layering transition of the particles at a surface. This effect can be modulated by specific interactions, but its origin is mainly entropic, as it can occur also in purely repulsive, athermal systems. At high nanoparticle concentrations, such as those typical of OSCs, the theory predicts the formation of several nanoparticle-rich layers. The effect is stronger when the ratio between the diameter of the nanoparticles and that of the polymer segments is around two, close to that resulting from a coarse-grained model of P3HT:PCBM blends.[72]

In this work, we present a combined experimental and numerical study of bilayer devices with fixed PCBM and variable P3HT content. One BHJ device is also included for comparison purposes. Our study begins with the examination of optical absorption spectra by means of the Tranfer Matrix Method (TMM).[73,74] We assume a simple function for the PCBM concentration profile across the active layer, and obtain its parameters by comparison of the measured and calculated absorptions. Afterwards, information on the PCBM concentration profiles is also obtained by comparison of the measured and calculated[75] EQE spectra. Finally, we derive the Internal Quantum Efficiencies (IQE) by computing the relative efficiencies of exciton diffusion, exciton dissociation and charge collection.

2 Results and discussion

2.1 Device efficiencies and optical properties

Table 1 collects the relevant experimental parameters for the bilayers (P1–P5) and the BHJ (B6) considered in this study. The PCE was calculated by means of the following relationship:[4]

$$\mathrm{PCE} = \frac{J_{\mathrm{sc}} \cdot V_{\mathrm{oc}} \cdot \mathrm{FF}}{I_{\mathrm{AM1.5G}}} \quad (1)$$

where $I_{\mathrm{AM1.5G}}$ = 100 mW cm^{-2} is the incident power density according to the AM1.5G standard.[76] Our PCE values are comparable to those of Ayzner *et al.*[28] Upon increasing the P3HT content, the PCE increases reaching the maximum value for device P3 (2.79%). Compared to device P3, device P4 shows

Table 1 Overview of experimental device parameters: P3HT (PCBM) nominal layer thicknesses ($L_{P3HT(PCBM)}$), volume ratios, short-circuit current density from the solar simulator (J_{sc}), open-circuit voltage (V_{oc}), fill factor (*FF*) and power conversion efficiency (PCE%)

Device	$L_{P3HT}:L_{PCBM}$ [nm]	J_{sc} [mA cm^{-2}]	V_{oc} [V]	FF	PCE (%)
P1	40 : 44 (0.9 : 1)	6.38	0.57	0.66	2.41
P2	50 : 44 (1.1 : 1)	6.55	0.59	0.71	2.74
P3	90 : 44 (2.0 : 1)	6.64	0.59	0.71	2.79
P4	146 : 44 (3.3 : 1)	6.75	0.61	0.63	2.59
P5	194 : 44 (4.4 : 1)	4.78	0.61	0.47	1.37
B6	88[a] (1.1 : 1)	6.71	0.55	0.69	2.55

[a] Total device thickness.

higher values of both J_{sc} and V_{oc}, but its overrall efficiency is lower due to a poorer fill factor. A further increase in P3HT film thickness does not affect V_{oc}, but appears to have a negative impact on both J_{sc} and FF. This makes P5 the least performing device in the set. Finally, the BHJ device, B6, has the volume ratio, the fill factor and PCE between those of P1 and P2, but a V_{oc} value lower than both.

In order to rationalize the above observations, we begin from the spectrally resolved total device absorption, A^{tot}. We consider the range between 300 and 650 nm, where P3HT:PCBM blends absorb significantly. To analyse the experimental data, we used the one-dimensional Transfer Matrix Method (TMM),[73,74] which can model the active layer absorption taking into account optical interference effects. The device is described as a collection of layers sequentially stacked on the top of each other along the *z* axis (see Fig. 1). The thicknesses and complex refractive indices of the layers comprising the solar cell must be provided as input to the TMM model. In this work, the optical constants of all materials were determined by variable angle spectroscopic ellipsometry, as detailed in the Experimental section. Published data[77] were preferred only for P3HT, due to better agreement with the experimental device absorption spectra (see ESI† for details). It is well known that the P3HT absorption is quite sensitive to its degree of order.[78] The data employed in our final fits[77] correspond to P3HT samples with relatively high crystallinity, consistently with the extensive annealing process carried out on our films (see the Experimental section).

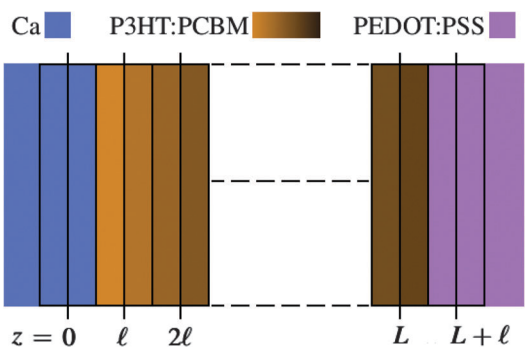

Fig. 1 Sketch of the photoactive layer scheme used in TMM calculations. Note that $L = L_{P3HT} + L_{PCBM}$. Cathode (anode) positions are set at $z = 0(L)$. The position of the mid points of each layer along the z axis is shown. For clarity, the remaining layers have been omitted.

The photoactive film was represented as a set of consecutive layers of thickness $\ell = 2$ nm. The PCBM volume fraction at the centre of each layer was represented by a sigmoid function:

$$f(z) = \frac{1}{1 + b \cdot e^{c(z-d)}}. \quad (2)$$

The complex refractive index of each layer was calculated by averaging those of the pure components ($\varepsilon_{P3HT(PCBM)}$):

$$\varepsilon(z,\lambda) = f(z)\varepsilon_{PCBM}(\lambda) + (1 - f(z))\varepsilon_{P3HT}(\lambda). \quad (3)$$

The parameters *b* and *d* were chosen to keep the overall amount of PCBM constant (see ESI† for details). The parameter *c* was varied to describe a variety of PCBM distributions: conventional bilayers ($c > 0$), uniform and homogeneous bulk-heterojunctions ($c = 0$). Negative values of *c* were also considered to account for the accumulation of PCBM at the PEDOT:PSS layer, already observed in some BHJs.[59,60,79]

Fig. 2 shows the experimental and fifty simulated absorption profiles of each device. These were obtained increasing *c* by 0.008 nm^{-1} in the range [+0.2, −0.2] nm^{-1}. Devices P1, P2 and B6 (top panel) show similar experimental absorption spectra. The comparison with the simulated profiles suggests a fairly uniform distribution of PCBM across the active film ($c \simeq 0$). This is evidenced by the intensity of the broad spectral feature at 400 nm, and by the peaks at around 520, 550, and 600 nm, which are associated with the π–π* transitions in ordered films of pristine, regioregular P3HT.[78,80–83] The best least-squares fits have been highlighted in Fig. 2, and the corresponding values of *c* are reported in Table 2, together with the associated root-mean-square deviations (σ_A). The negative values of *c* obtained suggest the possibility of PCBM accumulation at the PEDOT:PSS anode in these thin devices (<100 nm). As discussed in the Introduction, this is consistent with other experimental work on BHJ devices and polymer–nanoparticle blends, as well as some theoretical analyses.

Evaluating the PCBM distribution on the basis of optical modeling is more difficult for the thicker devices (bottom panel),

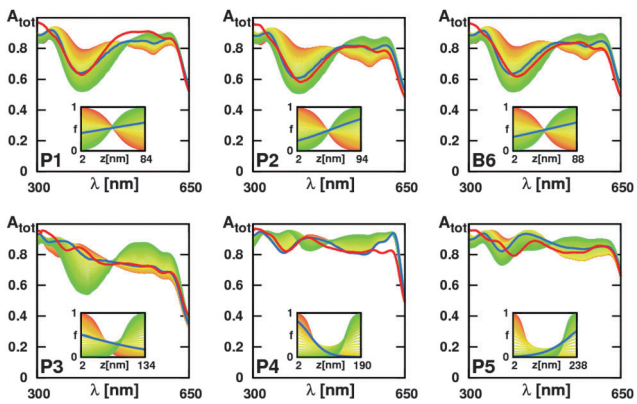

Fig. 2 Experimental (red) and simulated total absorption spectra for each device. A color gradient is used to highlight the change in absorption on going from $c > 0$ (orange) to $c < 0$ (green). The insets show the corresponding PCBM volume fractions, $f(z)$. Best least-squares fits are highlighted in blue.

Table 2 Values of b, c, and d (see eqn (2)) obtained from least-square fits of the experimental absorption data. The values of b and d were estimated as explained in the ESI. Root-mean-square deviations are listed in the last column

Device	b	c [nm^{-1}]	d [nm]	σ_A ($\times 10^{-2}$)
P1	0.91	−0.024	20.91	3.93
P2	1.14	−0.048	23.78	3.16
P3	2.05	0.024	32.48	2.65
P4	3.32	0.080	34.67	4.44
P5	4.41	−0.040	72.78	4.29
B6	1.09	−0.032	22.12	3.69

Table 3 Experimental values of η_A and J_{sc}^A calculated setting λ_1 = 300 nm and λ_2 = 650 nm. In all cases, the parasitic absorption was calculated assuming an uniform PCBM distribution across the active layer

Device	η_A [%]	J_{sc}^A [mA cm^{-2}]
P1	67.4	11.329
P2	61.1	10.282
P3	63.0	10.596
P4	75.6	12.724
P5	78.6	13.127
B6	62.5	10.502

as the simulated absorption becomes less sensitive to the active layer composition. For device P3 and P4, the simulations suggest the possibility of a small and positive PCBM concentration gradient (see Table 2). For device P5, a negative value of c is obtained again. The differences between simulation and experiment for devices P4 and P5 suggest that the results of optical fitting can only be indicative in these cases. This is further confirmed by the values of σ_A, which were the highest in the set. Different factors can be responsible for this outcome. The PCBM volume fraction in thick devices can differ[33] by that described by eqn (2). Other factors can be the approximations made in calculating the refractive indices (see eqn (3)), and the fact that the optical model does not account for diffuse scattering nor the spatially-dependent optical constants of the active layer.[77] In any case, the comparison between the experimental and numerical data always indicates a substantial mixing between PCBM and P3HT. This conclusion is supported by a number of studies,[32,33,37–39] and is consistent with our simulations of the EQE spectra, to be discussed below.

Because of their dependence on wavelength, the device absorption spectra are not well suited to compare different devices. A simpler and more convenient measure of the absorption efficiency can be defined as follows:

$$\eta_A = \frac{J_{sc}^A}{J_{sc}^{MAX}}. \quad (4)$$

Here J_{sc}^{MAX} is the maximum current density that could be extracted from a device (assuming λ_1 = 300 nm and λ_2 = 650 nm):[14]

$$J_{sc}^{MAX} = \frac{q}{hc}\int_{\lambda_1}^{\lambda_2} P_{AM1.5G}(\lambda)\lambda d\lambda = 16.813 \text{ mA cm}^{-2}, \quad (5)$$

where $P_{AM1.5G}$ is the AM1.5G solar irradiance,[76] q is the elementary charge, h is Planck's constant and c the speed of light *in vacuo*. J_{sc}^A is the current density that the device would generate at short-circuit, assuming that all the photons absorbed within the active layer contribute to the photocurrent:

$$J_{sc}^A = \frac{q}{hc}\int_{\lambda_1}^{\lambda_2} A^{act}(\lambda)\ P_{AM1.5G}(\lambda)\lambda d\lambda. \quad (6)$$

The active layer absorption can be obtained by subtracting the parasitic absorption by the electrodes (A^{prs}) from A^{tot}:[77]

$$A^{act}(\lambda) = A^{tot}(\lambda) - A^{prs}(\lambda). \quad (7)$$

The value of A^{prs} depends only slightly on the PCBM distribution. Here, A^{prs} was calculated setting c = 0 in eqn (2).

Table 3 collects the calculated values of J_{sc}^A and η_A. The absorption efficiency decreases on going from device P1 to P2. Beyond this point, it increases with the P3HT content, to reach a value of 78.6% for device P5. To better understand this result, we estimated the values of η_A for devices with gradually increasing P3HT content using the TMM model. In order to compare across devices with different thicknesses, a uniform PCBM distribution was assumed in these calculations. As shown in Fig. 3, these simulations interpolate well the experimental values. It is interesting to note that η_A reaches a maximum value for $L \approx 210$ nm, which is about five times the nominal PCBM thickness (44 nm). The 4 : 1 ratio between P3HT and PCBM is close to that found by Ayzner and coworkers,[28] for optimally efficient bilayers with nominal PCBM thicknesses of 22 and 34 nm. However, even though devices P4 and P5 show the highest values of η_A, they do not have the highest PCEs. This suggests that the "4 : 1 rule" is not completely general and there is a more complex relationship between bilayer efficiency and composition. In other words, optical absorption does not represent the main limit to the efficiency of the devices with high P3HT content.

Fig. 4 displays the experimental EQE profiles of the investigated devices. As one can see, the devices with lowest P3HT content (*e.g.*, P1, P2 and B6) show quite similar EQE spectra, characterized by peak values of around 520 nm. The shoulder at 615 nm, whose formation is promoted by thermal annealing,[59,82,84] also visible in the EQE profiles of the remaining devices. In P3, P4, and P5,

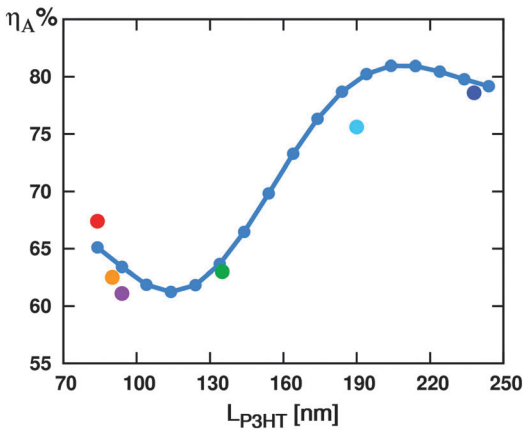

Fig. 3 Average absorption efficiencies calculated by the TMM, as a function of the active layer thickness L. The values of η_A from Table 3 are also reported. For comparison purposes, an uniform PCBM distribution across the active layer has been assumed.

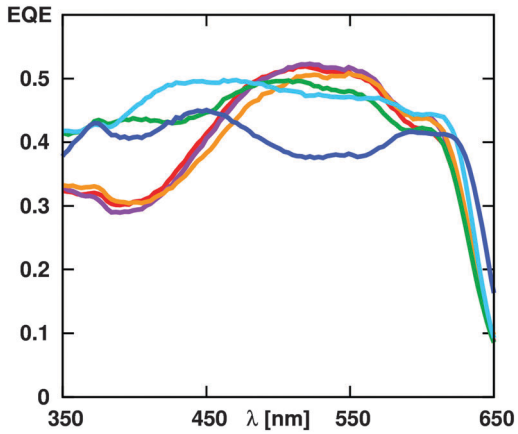

Fig. 4 EQE profiles of the investigated devices.

however, higher EQE values are observed at short wavelengths, due to enhanced optical absorption (see Fig. 1).

A deeper analysis of the bilayer efficiencies calls into play other factors, collectively described by the IQE, associated with charge and exciton transport. Spectrally resolved IQE profiles can be obtained by combining the active layer absorption and the EQE:[77]

$$\mathrm{IQE}(\lambda) = \frac{\mathrm{EQE}(\lambda)}{A^{\mathrm{act}}(\lambda)}. \tag{8}$$

The results are shown in Fig. 5. The IQE spectrum is expected to have a flat profile in a device where exciton diffusion and charge transport are equally efficient within the D and A materials.[85] Indeed, the IQE is almost flat for device P1. For P2 and P3, the IQE decreases in the region below 400 nm, where PCBM absorbs. This suggests that exciton transport might be less efficient in PCBM than in P3HT.[85] We shall briefly return to this point later on. A further increase in the P3HT content decreases the IQE at all wavelengths, leading to a significantly poorer performance of P5.

Detailed interpretation of IQE(λ) can be difficult and therefore it is preferable to introduce a spectrally averaged IQE, η_{IQE}.

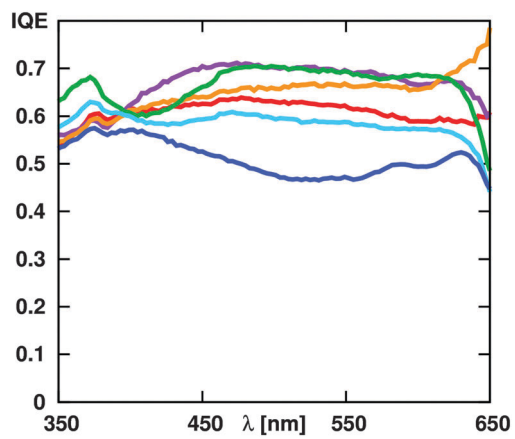

Fig. 5 IQE profiles of the investigated devices.

Instead of integrating eqn (8), which suffers from fluctuations in $A^{\mathrm{act}}(\lambda)$, it is preferable to define it as follows:

$$\eta_{\mathrm{IQE}} = \frac{J_{\mathrm{sc}}^{\mathrm{EQE}}}{J_{\mathrm{sc}}^{A}}, \tag{9}$$

where $J_{\mathrm{sc}}^{\mathrm{EQE}}$ is the short-circuit current density, calculated integrating the EQE over the solar spectrum:

$$J_{\mathrm{sc}}^{\mathrm{EQE}} = \frac{q}{hc}\int_{\lambda_1}^{\lambda_2} \mathrm{EQE}(\lambda) P_{\mathrm{AM1.5G}}(\lambda)\lambda \mathrm{d}\lambda. \tag{10}$$

The spectrally averaged external quantum efficiency, η_{EQE}, can be calculated combining eqn (4) and (9):

$$\eta_{\mathrm{EQE}} = \eta_A \cdot \eta_{\mathrm{IQE}} = \frac{J_{\mathrm{sc}}^{\mathrm{EQE}}}{J_{\mathrm{sc}}^{\mathrm{MAX}}}, \tag{11}$$

taking the η_A values from Table 3.

The values of η_{IQE} and η_{EQE} are listed in Table 4. Except for the thinnest device (P1), increasing the P3HT content decreases η_{IQE}. This loss is, nonetheless, compensated by the increase in optical absorption efficiency, so that the values of η_{EQE} for devices P4 and P5 remain close to 40%. The value of η_{IQE} for device B6 is comparable to that of P2 and P3.

The value of $J_{\mathrm{sc}}^{\mathrm{EQE}}$ obtained from eqn (10), and reported in Table 5, is often correlated with the short-circuit current density under the solar simulator.[14] However, the monochromatic illumination intensity in EQE experiments is typically in the nanowatt regime (10^{-4}–10^{-3} mW cm^{-2}), seven orders of magnitude smaller than that used in the standard J–V measurements.[86] This results in a far lower charge carrier density, so that we may expect $J_{\mathrm{sc}}^{\mathrm{EQE}} \simeq J_{\mathrm{sc}}$ only in devices where bimolecular recombination losses are negligible.[50] The second column of Table 5 contains the ratios $J_{\mathrm{sc}}/J_{\mathrm{sc}}^{\mathrm{EQE}}$. These indicate that bimolecular recombination plays a significant role at short-circuit only in the thickest device (P5). This conclusion is confirmed by the

Table 4 Values of η_{IQE} and η_{EQE} obtained from experimental data and calculated parasitic absorptions

Device	η_{IQE} [%]	η_{EQE} [%]
P1	60.97	41.04
P2	67.56	41.30
P3	66.73	42.15
P4	58.11	44.00
P5	49.88	39.45
B6	65.13	40.68

Table 5 Device parameters obtained from experimental data and calculated parasitic absorptions. The value of η_{ED} has been estimated *via* eqn (12) (see the text)

Device	$J_{\mathrm{sc}}^{\mathrm{EQE}}$ [mA cm^{-2}]	$J_{\mathrm{sc}}/J_{\mathrm{sc}}^{\mathrm{EQE}}$ [%]	η_{ED} [%]
P1	6.903	92.4	77.6
P2	6.953	94.2	84.4
P3	7.086	93.6	83.9
P4	7.400	91.2	75.0
P5	6.594	72.4	81.1
B6	6.839	98.0	78.2

measured dependence of the short-circuit current on the incident light intensity I. Fitting the response by the power law $J_{sc} \propto I^{\alpha}$, we found this to be almost linear for all devices ($\alpha = 0.98$), except for P5, which displayed a sublinear dependence ($\alpha = 0.92$).

So far, we have shown that η_{IQE} does not exceed 70% for the devices under investigation and, for most of them, this limit cannot be ascribed to bimolecular recombination processes. To further clarify the origin of IQE losses, we assume that η_{IQE} can be written as the product of three factors:[85,87]

$$\eta_{IQE} = \eta_{ED}\eta_{GP}\eta_{CC}. \quad (12)$$

These terms represent the efficiencies of exciton diffusion toward the D/A interface (ED), generation of geminate pairs upon exciton dissociation (GP), and collection of free charge carriers at the corresponding electrodes (CC). Their values can be estimated on the basis of our results and the available literature. According to the previous paragraph, η_{CC} can be approximated as J_{sc}/J_{sc}^{EQE}. Following the work of Howard *et al.*,[50] we may set $\eta_{GP} = 0.85$, thereby assuming that 15% of geminate pairs are lost soon after their formation, regardless of the device thickness and morphology. The resulting values of η_{ED}, reported in last column of Table 5, show that about 80% of the excitons generated by light harvesting reach the D/A interface. These results may be summarized by saying that exciton diffusion and geminate recombiantion are the main IQE loss factors in most devices. Bimolecular recombination, conversely, plays a minor role at short circuit, and severely affects only device P5.

2.2 Device simulations

In the previous section, we have highlighted the possibility of PCBM accumulation at the anode in the thinner bilayer devices. To further test this finding we performed numerical simulations of the EQE spectra. These were calculated by combining the TMM model for light absorption (with the AM1.5G spectrum between 300 and 650 nm, with a 3 nm window) with our three-dimensional master equation (3DME) approach.[75,88] This method can simulate explicitly the dynamics of excitons, geminate pairs and free charges but, to simplify the model and minimize the number of assumptions, only the exciton-related processes were simulated in this work. The pair and charge dynamics were taken into account implicitly, through the geminate recombination and charge collection efficiencies derived in the previous section (*i.e.*, we set $\eta_{GP} = 0.85$ and took $\eta_{CC} = J_{sc}/J_{sc}^{EQE}$ from Table 5). The EQE spectra were then calculated as follows:

$$EQE(\lambda) \simeq \frac{G_{sc}^{ED}(\lambda)}{G^{PH}}\eta_{GP}\eta_{CC}, \quad (13)$$

where G_{sc}^{ED} is the geminate pair generation rate from the 3DME simulations and $G^{PH} = P_{AM1.5G}(\lambda)\lambda/hc$ is the spectral photon flux. In all calculations, the exciton diffusion length and the coefficient were set to 4.5 nm and 1.33×10^{-4} cm^2 s^{-1}, respectively. These values are consistent with those of Cook *et al.*[89] for PCBM, and comparable to those from a number of studies on pristine P3HT.[90–94]

The photoactive layer was represented by a three-dimensional network of A and D sites with spacing $\ell = 2$ nm (equal to that used in the optical data analysis). Periodic boundary conditions were applied to the simulation box along the x and y axes, with lengths of 40 nm. Eqn (2) was used to model the PCBM volume fraction along the z axis and calculate the exciton generation rates. The distribution of A and D sites along the x and y axes was determined assuming the existence of well-defined, phase-separated but percolating PCBM domains within a pure P3HT matrix. This assumption was necessary in order to limit the freedom in the choice of the morphologies. Preliminary simulations, performed to asses the relationship between the model parameters and the EQE spectrum, revealed that the parameter c in eqn (2) had the largest influence on the EQE profile. At a given value of c, the distribution of A and D sites along the x and y axes, conversely, was found to affect significantly only the EQE intensity, due to the change in the extent of the D/A interface, and the exciton dissociation efficiency.

Hereafter, we shall compare the results of EQE simulations performed for two sets of parameters. The first set (S_A, hereafter) was drawn from Table 2, and refers to the TMM fits to the absorption spectra. The second set (S_{EQE}, hereafter) was obtained by optimizing c iteratively by comparison between simulated and experimental EQE spectra. In all calculations, the morphology parameters were also optimized to match the experimental EQE intensity as closely as possible. Further details about these simulations can be found in the ESI.†

Fig. 6 compares the simulated and the experimental EQE profiles. Table 6 collects S_{EQE} parameters. For devices P1, P2, and B6, S_{EQE} parameters were similar (P1) or coincident (P2 and B6) to S_A ones. For thicker devices, the two sets of c values were substantially different. For devices P3 and P4 negative values of c were found to better describe the experimental behavior. For device P4, morphology optimization (see ESI†) did not significantly improve the EQE spectrum. Finally, for device P5, a uniform PCBM distribution $c = 0$ gave better results than that resulting from the TMM fit ($c = -0.040$). The results of these calculations likely exclude the possibility of high positive, or negative, concentration gradients in P3HT:PCBM blends,

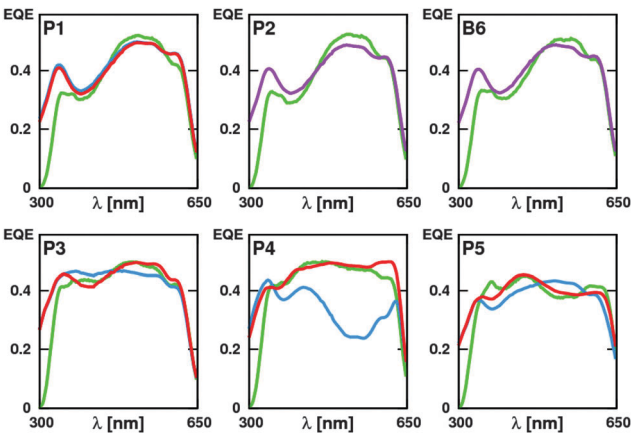

Fig. 6 Comparison between experimental (green) and simulated EQE profiles, corresponding to S_A (blue), and S_{EQE} (red). For coincident values of c, one best-fitting profile was obtained (purple).

Table 6 Values of b, c, and d best fitting the experimental EQE data (S_{EQE}). The values of b and d were estimated as explained in the ESI

Device	b	c [nm^{-1}]	d [nm]
P1	0.91	−0.040	20.86
P2	1.14	−0.048	23.78
P3	2.05	−0.020	34.77
P4	3.32	−0.010	49.51
P5	4.41	0.0	0.0
B6	1.09	−0.032	22.12

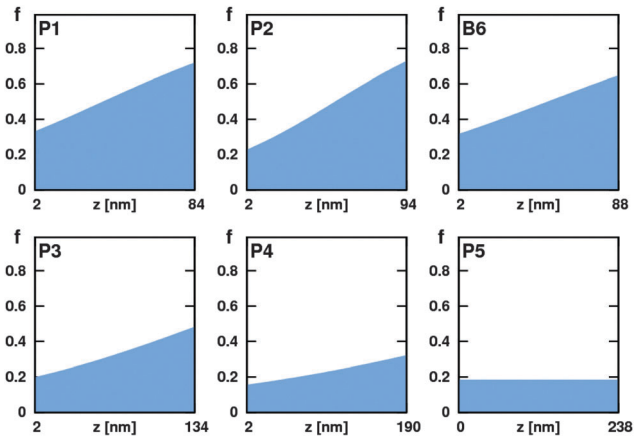

Fig. 7 PCBM volume fractions (f) calculated according to eqn (2) and the values of c reported in Table 5.

in favor of smooth and uniform distributions of both components across the active layer.

Fig. 7 shows the PCBM volume fractions corresponding to S_{EQE} parameters. It is interesting to note that, except for device P5, all values of c are small and negative, and a significant fraction ($f \simeq 0.7$) of PCBM is in contact with the anode of devices P1, P2 and B6. Our PCBM fractions look similar to those observed by Campoy-Quiles *et al.*[59] in P3HT:PCBM films deposited on a PEDOT:PSS/SiO_2 substrate. The idea of P3HT:PCBM interdiffusion is also supported by other studies,[33,38,95] where, however, no clear evidence of PCBM accumulation at the anode was found. This difference can be due to the fact that the experimental characterization of the PCBM distribution was perfomed on systems different than our devices (in particular, P3HT:PCBM films deposited on SiO_2/Si, or Si, substrates). At the same time, these studies suggest that step-wise functions could better describe the PCBM fraction in annealed bilayers than eqn (2). The implementation of these models will be addressed in future studies.

3 Summary and conclusions

In this work, we have examined the effect of the donor content on the performance of sequentially deposited P3HT:PCBM bilayers, with the aim of understanding the interplay between the different factors responsible for device efficiency. The analysis of the optical absorption data, using a flexible model to describe the vertical concentration profiles, has shown the occurrence of significant mixing between P3HT and PCBM, in agreement with much current evidence. In both bulk heterojunction and bilayer devices with an active layer thikness of 100 nm or less, our best fits to the optical data highlighted the accumulation of PCBM at the interface with the anode.

The evaluation of spectrally averaged quantities has shown that increasing the P3HT content (at fixed PCBM content) improves the photon absorption but tends to depress the IQE. The trade-off between these factors sets the maximum power conversion efficency at about 2.8% and the optimal P3HT:PCBM volume ratio at 2 : 1. This ratio contrasts with that of 4 : 1 reported in the literature for devices with lower PCBM content, suggesting a more complex relationship between device efficiency and photoactive layer composition. Combining our results and literature estimates, we have shown that exciton diffusion and geminate recombination can be the main factors limiting the IQE ($\eta_{IQE} < 70\%$). Conversely, bimolecular recombination effects are small at short-circuit, and play a role only in the device with the highest P3HT content. This finding is consistent with recent work of Shuttle *et al.*,[96] and suggests that "bilayers" and BHJs behave similarly, in this respect.

In the last part of the paper, we have used a variant of our 3DME model[75,88] to simulate the EQE spectra. Only the exciton dynamics has been simulated explicitly, while the pair and charge dynamics have been treated implicitly *via* geminate recombination and charge collection efficiencies. The results from our fits to the EQE data agree with those from optical data analysis for the devices with lower P3HT content (P1, P2, and B6). Smoother and more uniform PCBM fractions were found for the remaining devices, similar to those observed experimentally.[39]

Our results suggest that even the best devices have a significant fraction of PCBM at the interface with the PEDOT:PSS anode. This finding is somewhat unexpected for bilayers[31] but, as discussed in the Introduction, it is consistent with the ability of PCBM to diffuse through P3HT[28,41] and with many results demonstrating a vertical concentration gradient in BHJs.[30,41,59–61] It seems to be related to a general tendency of small nanoparticles to accumulate at polymer–solid interfaces,[67,68] which has been confirmed also by statistical mechanical analyses of the behaviour of simple polymer–nanoparticle models.[69,70]

4 Experimental

4.1 Device preparation

For the present study, we considered five ITO/PEDOT:PSS/P3HT/PCBM/Ca/Al bilayers and one BHJ. The bilayers were prepared starting from a transparent anode made by a pre-patterned ITO glass (Kintec, 15 Ω sq^{-1}). A 60 nm hole-transport layer of PEDOT–PSS (Stark, VP Al 4083) was deposited on top by spin coating dried on a hot-plate at 100 °C for 5 minutes in air and then inserted in a glove-box for further device assembling. The active layers were deposited by spin coating following a procedure developed by Ayzner *et al.*[28] The P3HT (Plexcore OS2100) with high molecular weight (M_n: 62 602 M_w: 119 010) and 99% regioregularity was purchased from Plextronics.

The polymer was dissolved in *o*-dichlorobenzene at concentrations of 10, 15, 20, 25 mg ml^{-1}. The solutions were kept at 50 °C and stirred overnight prior to spin coating onto the PEDOT:PSS/ITO substrates. The first solution was spin coated at two different rates. The resulting P3HT film thicknesses, measured using a profilometer (Dektak), were 40 ± 2, 50 ± 2, 90 ± 3, 146 ± 2, 194 ± 2 nm. We shall, hereafter, denote these devices P1–P5 (see Table 1). After drying for at least 30 minutes, a PCBM overlayer (Solenne b.v.) of 44 ± 4 nm was deposited from dichloromethane (10 mg ml^{-1}). Prior to cathode evaporation, the deposited films were annealed on a hot plate at 150 °C for 30 minutes. The electrodes, 20 nm Ca and 100 nm Al, were thermally evaporated through a shadow mask of 6 mm^2, in a vacuum chamber at 2 × 10^{-6} mbar. A bulk-heterojunction P3HT:PCBM device (1 : 1.22 w : w, 1.1 : 1 v : v), hereafter B6, was also prepared. The active layer, 88 ± 2 nm, was deposited from *o*-dichlorobenzene and solvent annealed by slow drying into a petri dish for 2 hours. Then a thermal treatment on a hot plate at 90 °C for 5 minutes was carried out prior to the cathode deposition.

4.2 Device characterization

The current density–voltage (*J*–*V*) characteristics of all cells were measured at room temperature inside the glove box in a nitrogen atmosphere, using a Keithley 2600 sourcemeter under 100 mW cm^{-2} solar simulation (AM1.5 ABET Sun 2000), as measured using a calibrated KG5 + Si cell. The EQE spectral responses were recorded by a Xe lamp dispersing through a monochromator, using a Si calibrated photodiode to measure the incident light power intensity at each wavelength. The devices were taken outside the glove box for the EQE measurements, after mounting them on a sealed cell to avoid moisture and oxygen exposure. Device optical absorption spectra were measured in reflection mode. An integrating sphere was used to capture the scattered light and increase accuracy. The white light source and the monochromator were the same as those used to measure the EQE spectra.

4.3 Optical constant measurements

The optical constants for ITO, PEDOT:PSS, P3HT, and PCBM were determined with variable angle ellipsometry using a Woollam VASE ellipsometer. Published data[77] were used for Ca and Al. Each material was characterized individually in the range from 300 to 900 nm. At least two incident angles for each sample were considered in order to increase the quality of the measurements. PEDOT:PSS, P3HT, and PCBM samples were prepared by deposition on a Si substrate, under conditions similar to those used for the preparation of solar cells (see above). Use of Si instead of the glass/ITO substrate allowed us to remove backside reflection effects and improve sensitivity. ITO was deposited on glass. The thickness of each layer was determined by profilometry and used as a constant in the fitting procedure. Different models were used to fit the data and calculate the optical constants. A Cauchy model was used for PEDOT:PSS, while a general oscillator model for the absorbing media. As discussed in the ESI,† published P3HT data[77] were used instead of ours in all TMM simulations.

Acknowledgements

We thank Prof. Stefano Valdo Meille for valuable comments and useful discussions. We benefitted from computer time kindly provided by Regione Lombardia and CINECA (LISA and ISCRA grants).

References

1 C. J. Brabec, S. Gowrisanker, J. J. M. Halls, D. Laird, S. Jia and S. P. Williams, *Adv. Mater.*, 2010, **22**, 3839–3856.
2 J. Nelson, *Mater. Today*, 2011, **14**, 462–470.
3 R. F. Service, *Science*, 2011, **332**, 293.
4 R. Po, M. Maggini and N. Camaioni, *J. Phys. Chem. C*, 2010, **114**, 695–706.
5 N. Espinosa, M. Hosel, M. Jorgensen and F. C. Krebs, *Energy Environ. Sci.*, 2014, **7**, 855–866.
6 G. Li, R. Zhu and Y. Yang, *Nat. Photonics*, 2012, **6**, 153–161.
7 M. T. Dang, L. Hirsch, G. Wantz and J. D. Wuest, *Chem. Rev.*, 2013, **113**, 3734–3765.
8 W. Yin and M. Dadmun, *ACS Nano*, 2011, **5**, 4756–4768.
9 S. Cook, A. Furube, R. Katoh and L. Han, *Chem. Phys. Lett.*, 2009, **478**, 33–36.
10 O. V. Mikhnenko, H. Azimi, M. Scharber, M. Morana, P. W. M. Blom and M. A. Loi, *Energy Environ. Sci.*, 2012, **5**, 6960–6965.
11 P. E. Shaw, A. Ruseckas and I. D. W. Samuel, *Adv. Mater.*, 2008, **20**, 3516–3520.
12 M. Sim, J. Shin, C. Shim, M. Kim, S. B. Jo, J.-H. Kim and K. Cho, *J. Phys. Chem. C*, 2014, **118**, 760–766.
13 S. M. Menke and R. J. Holmes, *Energy Environ. Sci.*, 2014, **7**, 499–512.
14 G. Dennler, M. C. Scharber and C. J. Brabec, *Adv. Mater.*, 2009, **21**, 1323–1338.
15 G. Li, V. Shrotriya, Y. Yao, J. Huang and Y. Yang, *J. Mater. Chem.*, 2007, **17**, 3126–3140.
16 Y. Xiaohan and U. Ashraf, *Renewable Sustainable Energy Rev.*, 2014, **30**, 324–336.
17 D. Chirvase, J. Parisi, J. C. Hummelen and V. Dyakonov, *Nanotechnology*, 2004, **15**, 1317.
18 A. Ng, X. Liu, C. H. To, A. B. Djurišić, J. A. Zapien and W. K. Chan, *ACS Appl. Mater. Interfaces*, 2013, **5**, 4247–4259.
19 Y. Liang and L. Yu, *Acc. Chem. Res.*, 2010, **43**, 1227–1236.
20 S. H. Park, A. Roy, S. Beaupré, S. Cho, N. Coates, J. S. Moon, D. Moses, M. Leclerc, K.-H. Lee and A. J. Heeger, *Nat. Photonics*, 2009, **3**, 297.
21 T.-Y. Chu, J. Lu, S. Beaupré, Y. Zhang, J.-R. Pouliot, S. Wakim, J. Zhou, M. Leclerc, Z. Li, J. Ding and Y. Tao, *J. Am. Chem. Soc.*, 2011, **133**, 4250–4253.
22 Y. Y. Liang, Z. Xu, J. B. Xia, S. T. Tsai, Y. Wu, G. Li, C. Ray and L. P. Yu, *Adv. Mater.*, 2010, **22**, E135–E138.
23 E. Verploegen, R. Mondal, C. J. Bettinger, S. Sok, M. F. Toney and Z. Bao, *Adv. Funct. Mater.*, 2010, **20**, 3519–3529.

24 J. H. Park, J. S. Kim, J. H. Lee, W. H. Lee and K. Cho, *J. Phys. Chem. C*, 2009, **113**, 17579–17584.
25 J. Peet, M. L. Senatore, A. J. Heeger and G. C. Bazan, *Adv. Mater.*, 2009, **21**, 1521–1527.
26 Y. Xie, Y. Bao, J. Du, C. Jiang and Q. Qiao, *Phys. Chem. Chem. Phys.*, 2012, **14**, 10168–10177.
27 D. Chen, A. Nakahara, D. Wei, D. Nordlund and T. P. Russell, *Nano Lett.*, 2011, **11**, 561–567.
28 A. L. Ayzner, C. J. Tassone, S. H. Tolbert and B. J. Schwartz, *J. Phys. Chem. C*, 2009, **113**, 20050–20060.
29 D. O'Brien, M. Weaver, D. G. Lidzey and D. Bradley, *Appl. Phys. Lett.*, 1996, **69**, 881–883.
30 A. Loiudice, A. Rizzo, G. Latini, C. Nobile, M. de Giorgi and G. Gigli, *Sol. Energy Mater. Sol. Cells*, 2012, **100**, 147–152.
31 K. H. Lee, P. E. Schwenn, A. R. G. Smith, H. Cavaye, P. E. Shaw, M. James, K. B. Krueger, I. R. Gentle, P. Meredith and P. L. Burn, *Adv. Mater.*, 2010, **23**, 766.
32 V. S. Gevaerts, L. J. A. Koster, M. M. Wienk and R. a. J. Janssen, *ACS Appl. Mater. Interfaces*, 2011, **3**, 3252.
33 N. D. Treat, M. A. Brady, G. Smith, M. F. Toney, E. J. Kramer, C. J. Hawker and M. L. Chabinyc, *Adv. Energy Mater.*, 2010, **1**, 82.
34 D. H. Wang, D.-G. Choi, O. O. Park and J. H. Park, *J. Mater. Chem.*, 2010, **20**, 4910–4915.
35 B. Tremolet de Villers, C. J. Tassone, S. H. Tolbert and B. J. Schwartz, *J. Phys. Chem. C*, 2009, **113**, 18978–18982.
36 A. M. Nardes, A. L. Ayzner, S. R. Hammond, A. J. Ferguson, B. J. Schwartz and N. Kopidakis, *J. Phys. Chem. C*, 2012, **116**, 7293.
37 J. Moon, C. Takacs, Y. Sun and A. J. Heeger, *Nano Lett.*, 2011, **11**, 1036.
38 D. Chen, F. Liu, C. Wang, A. Nakahara and T. P. Russell, *Nano Lett.*, 2011, **11**, 2071–2078.
39 C. W. Rochester, S. A. Mauger and A. J. Moulé, *J. Phys. Chem. C*, 2012, **116**, 7287–7292.
40 H. Chen, S. Hu, H. Zang, B. Hu and M. Dadmun, *Adv. Funct. Mater.*, 2013, **23**, 1701–1710.
41 K. H. Lee, Y. Zhang, P. L. Burn, I. R. Gentle, M. James, A. Nelson and P. Meredith, *J. Mater. Chem. C*, 2013, **1**, 2593–2598.
42 A. L. Ayzner, S. C. Doan, B. Tremolet de Villers and B. J. Schwartz, *J. Phys. Chem. Lett.*, 2012, **3**, 2281–2287.
43 A. J. Moulé, J. B. Bonekamp and K. Meerholz, *J. Appl. Phys.*, 2006, **100**, 094503.
44 L. Zeng, C. W. Tang and S. H. Chen, *Appl. Phys. Lett.*, 2010, **97**, 053305.
45 J. D. Kotlarski, D. J. D. Moet and P. W. M. Blom, *J. Polym. Sci., Part B: Polym. Phys.*, 2011, **49**, 708–711.
46 D. W. Sievers, V. Shrotriya and Y. Yang, *J. Appl. Phys.*, 2006, **100**, 114509.
47 C. Groves, *Energy Environ. Sci.*, 2013, **6**, 3202–3217.
48 B. P. Lyons, N. Clarke and C. Groves, *Energy Environ. Sci.*, 2012, **5**, 7657–7663.
49 J. D. Servaites, M. A. Ratner and T. J. Marks, *Energy Environ. Sci.*, 2011, **4**, 4410–4422.
50 I. A. Howard, R. Mauer, M. Meister and F. Laquai, *J. Am. Chem. Soc.*, 2010, **132**, 14866–14876.
51 D. P. McMahon, D. L. Cheung and A. Troisi, *J. Phys. Chem. Lett.*, 2011, **2**, 2737–2741.
52 D. Caruso and A. Troisi, *Proc. Natl. Acad. Sci. U. S. A.*, 2012, **109**, 13498–13502.
53 C. Deibel, T. Strobel and V. Dyakonov, *Phys. Rev. Lett.*, 2009, **103**, 036402.
54 A. A. Bakulin, A. Rao, V. G. Pavelyev, P. H. M. van Loosdrecht, M. S. Pshenichnikov, D. Niedzialek, J. Cornil, D. Beljonne and R. H. Friend, *Science*, 2012, **335**, 1340–1344.
55 S. Gélinas, A. Rao, A. Kumar, S. L. Smith, A. W. Chin, J. Clark, T. S. van der Poll, G. C. Bazan and R. H. Friend, *Science*, 2014, **343**, 512–516.
56 G. Grancini, M. Maiuri, D. Fazzi, A. Petrozza, H.-J. Egelhaaf, D. Brida, G. Cerullo and G. Lanzani, *Nat. Mater.*, 2014, **12**, 29–33.
57 K. Vandewal, S. Albrecht, E. T. Hoke, K. R. Graham, J. Widmer, J. D. Douglas, M. Schubert, W. R. Mateker, J. T. Bloking, G. F. Burkhard, A. Sellinger, J. M. J. Fréchet, A. Amassian, M. K. Riede, M. D. McGehee, D. Neher and A. Salleo, *Nat. Mater.*, 2014, **13**, 63–68.
58 G. Raos, M. Casalegno and J. Idé, *J. Chem. Theory Comput.*, 2014, **10**, 364–372.
59 M. Campoy-Quiles, T. Ferenczi, T. Agostinelli, P. G. Etchegoin, Y. Kim, T. D. Anthopoulos, P. N. Stavrinou, D. D. C. Bradley and J. Nelson, *Nat. Mater.*, 2008, **7**, 158–164.
60 S. A. Mauger, L. Chang, S. Friedrich, C. W. Rochester, D. M. Huang, P. Wang and A. J. Moulé, *Adv. Funct. Mater.*, 2013, **23**, 1935–1946.
61 M. D. Clark, M. L. Jespersen, R. J. Patel and B. J. Leever, *ACS Appl. Mater. Interfaces*, 2013, **5**, 4799–4807.
62 A. C. Balazs, T. Emrick and T. P. Russell, *Science*, 2006, **314**, 1107–1110.
63 G. Allegra, G. Raos and M. Vacatello, *Prog. Polym. Sci.*, 2008, **33**, 683–731.
64 J. Jancar, J. Douglas, F. Starr, S. Kumar, P. Cassagnau, a. J. Lesser, S. Sternstein and M. Buehler, *Polymer*, 2010, **51**, 3321–3343.
65 M. Grzelczak, J. Vermant, E. Furst and L. Liz-Marzan, *ACS Nano*, 2010, **4**, 3591–3605.
66 L.-T. Yan and X.-M. Xie, *Prog. Polym. Sci.*, 2013, **38**, 369–405.
67 K. A. Barnes, A. Karim, J. F. Douglas, A. I. Nakatani, H. Gruell and E. J. Amis, *Macromolecules*, 2000, **33**, 4177–4185.
68 M. E. Mackay, Y. Hong, M. Jeong, S. Hong, T. P. Russell, C. J. Hawker, R. Vestberg and J. F. Douglas, *Langmuir*, 2002, **18**, 1877–1882.
69 E. S. McGarrity, A. L. Frischknecht and M. E. Mackay, *J. Chem. Phys.*, 2008, **128**, 154904.
70 A. L. Frischknecht, V. Padmanabhan and M. E. Mackay, *J. Chem. Phys.*, 2012, **136**, 164904.
71 V. Padmanabhan, A. L. Frischknecht and M. E. Mackay, *Macromol. Theory Simul.*, 2012, **21**, 98–105.
72 C.-K. Lee, C.-W. Pao and C.-W. Chu, *Energy Environ. Sci.*, 2011, **4**, 4124.
73 L. A. A. Pettersson, L. S. Roman and O. Inganäs, *J. Appl. Phys.*, 1999, **86**, 487–496.
74 P. Peumans, A. Yakimov and S. R. Forrest, *J. Appl. Phys.*, 2003, **93**, 3693–3723.

75 M. Casalegno, A. Bernardi and G. Raos, *J. Chem. Phys.*, 2013, **139**, 024706.
76 Web site for NREL's AM1.5 Standard Dataset, accessed 9 January 2014, http://rredc.nrel.gov/solar/spectra/am1.5.
77 G. F. Burkhard, E. T. Hoke and M. D. McGehee, *Adv. Mater.*, 2010, **22**, 3293–3297.
78 J. Clark, J.-F. Chang, F. C. Spano, R. H. Friend and C. Silva, *Appl. Phys. Lett.*, 2009, **94**, 163306.
79 G. Li, V. Shrotriya, J. Huang, Y. Yao, T. Moriarty, K. Emery and Y. Yang, *Nat. Mater.*, 2005, **4**, 864–868.
80 P. Vanlaeke, A. Swinnen, I. Haeldermans, G. Vanhoyland, T. Aernouts, D. Cheyns, C. Deibel, J. D'Haen, P. Heremans, J. Poortmans and J. Manca, *Sol. Energy Mater. Sol. Cells*, 2006, **90**, 2150–2158.
81 V. Shrotriya, J. Ouyang, R. J. Tseng, G. Li and Y. Yang, *Chem. Phys. Lett.*, 2005, **411**, 138–143.
82 Y. Kim, S. Cook, S. M. Tuladhar, S. A. Choulis, J. Nelson, J. R. Durrant, D. D. C. Bradley, M. Giles, I. McCulloch, C.-S. Ha and M. Ree, *Nat. Mater.*, 2006, **5**, 197–203.
83 R. Mauer, M. Kastler and F. Laquai, *Adv. Funct. Mater.*, 2010, **20**, 2085–2092.
84 K. Kim, J. Liu, M. A. G. Namboothiry and D. L. Carroll, *Appl. Phys. Lett.*, 2007, **90**, 63511.
85 G. F. Burkhard, E. T. Hoke, S. R. Scully and M. D. McGehee, *Nano Lett.*, 2009, **9**, 4037–4041.
86 S. R. Cowan, J. Wang, J. Yi, Y.-J. Lee, D. C. Olson and J. W. P. Hsu, *J. Appl. Phys.*, 2013, **113**, 154504.
87 K. Vandewal, S. Himmelberger and A. Salleo, *Macromolecules*, 2013, **46**, 6379–6387.
88 M. Casalegno, C. Carbonera, S. Luzzati and G. Raos, *Org. Electron.*, 2012, **13**, 750–761.
89 S. Cook, A. Furube, R. Katoh and L. Han, *Chem. Phys. Lett.*, 2009, **478**, 33–36.
90 O. V. Mikhnenko, H. Azimi, M. Scharber, M. Morana, P. W. M. Blom and M. A. Loi, *Energy Environ. Sci.*, 2012, **5**, 6960–6965.
91 P. E. Shaw, A. Ruseckas and I. D. W. Samuel, *Adv. Mater.*, 2008, **20**, 3516–3520.
92 H. Wang, H.-Y. Wang, B.-R. Gao, L. Wang, Z.-Y. Yang, X.-B. Du, Q.-D. Chen, J.-F. Song and H.-B. Sun, *Nanoscale*, 2011, **3**, 2280–2285.
93 J. E. Kroeze, T. J. Savenije, M. J. W. Vermeulen and J. M. Warman, *J. Phys. Chem. B*, 2003, **107**, 7696–7705.
94 L. Lüer, H.-J. Egelhaaf, D. Oelkrug, G. Cerullo, G. Lanzani, B.-H. Huisman and D. de Leeuw, *Org. Electron.*, 2004, **5**, 83–89.
95 F. Liu, Y. Gu, J. W. Jung, W. H. Jo and T. P. Russell, *J. Polym. Sci., Part B: Polym. Phys.*, 2012, **50**, 1018–1044.
96 C. G. Shuttle, R. Hamilton, B. C. ORegan, J. Nelson and J. R. Durrant, *Proc. Natl. Acad. Sci. U. S. A.*, 2010, **107**, 16448–16452.